

Experimentally Measured Effects of Incidence Angle on the Adiabatic and Overall Effectiveness of a Fully Cooled Turbine Airfoil With Shaped Showerhead Holes

Kyle Chavez

Department of Mechanical Engineering,
The University of Texas at Austin,
Austin, TX 78712
e-mail: Kyle.F.Chavez@utexas.edu

Thomas N. Slavens

Pratt & Whitney,
East Hartford, CT 06118
e-mail: Thomas.Slavens@pw.utc.com

David Bogard

Department of Mechanical Engineering,
The University of Texas at Austin,
Austin, TX 78712
e-mail: dbogard@mail.utexas.edu

Manufacturing and assembly variation can lead to shifts in the inlet flow incidence angles of a rotating turbine airfoil row. Understanding the sensitivity of the adiabatic film cooling effectiveness to a range of inlet conditions is necessary to verify the robustness of a cooling design. In order to investigate the effects of inlet flow incidence angles, adiabatic and overall effectiveness data were measured in a low speed linear cascade at 0 deg and 10 deg of the designed operating condition. Tests were completed at an inlet Reynolds number of $Re = 120,000$ and a turbulence intensity of $Tu = 5\%$ at the leading edge of the test article. Particle image velocimetry was used to verify the incident flow angle for each angle studied. The test section was first adjusted so that the pressure distribution and stagnation line of the airfoil matched those predicted by an aerodynamic computational fluid dynamics (CFD) model. IR thermography was then used to measure the adiabatic effectiveness levels of the fully cooled airfoil model with nine rows of shaped holes of varying construction and feed delivery. Measurements were taken over a range of blowing ratios and at a density ratio of $DR = 1.23$. This process was repeated for the two incidence angles measured, while the inlet pressure to the airfoil model was held constant for these incidence angle changes. Differences in laterally adiabatic effectiveness across the airfoil model were most evident in the showerhead, with changes as large as 0.2. The effect persisted most strongly at $s/D = \pm 35$ downstream of the stagnation row of holes, but was visible over the whole viewable area of 160 s/D . The effect was due to the stagnation line affecting the film at the showerhead row. Due to this effect, the showerhead was investigated in detail, including the effects of the stagnation line shift as well as the influence of the incidence angle on the overall effectiveness of the showerhead region. It was found that the stagnation line has the tendency to dramatically increase the near-hole adiabatic effectiveness levels when positioned within the breakout footprint of the hole. The effect persisted for the overall effectiveness study, since the hole spacing for this particular configuration was wide enough that the through hole convection was not completely dominant. This is the first study to present measured effectiveness values over both the pressure- and suction-side surfaces of a fully cooled airfoil for appreciably off-nominal incidence angles as well as examine adiabatic and overall effectiveness levels for a conical stagnation row of holes. [DOI: 10.1115/1.4036200]

Introduction

Early stage gas turbine airfoil components often utilize internal and film-cooling schemes in order to actively cool the components during operation. In order to investigate the effects of the film cooling on the external surface of the turbine component, the adiabatic effectiveness, η , can be measured. The adiabatic effectiveness of airfoil models has been studied extensively in the literature, and for incompressible flows is defined as

$$\eta = \frac{T_{\infty} - T_{aw}}{T_{\infty} - T_{c,exit}} \quad (1)$$

where T_{aw} is the adiabatic wall temperature, T_{∞} is the mainstream total temperature, and $T_{c,exit}$ is the temperature of the coolant exiting the holes.

A wealth of information regarding the studies on adiabatic effectiveness dating back to the 1960s is available in the literature. The majority of adiabatic effectiveness measurements have utilized simplified geometries such as flat plates or leading edge geometries, as they often reduce the complexities and number of variables affecting the hydrodynamics and aero thermal effects of the film cooling jets, and thus serve as excellent benchmark measurements (see Goldstein [1,2], Goldstein et al. [2], and Hartnett et al. [3] for examples). Since the first studies on film cooling, thousands of studies have been published, which investigate the effects of varying fluid properties, fluid flow rates, hole geometry, turbine component geometry, etc., on film cooling. As references, a useful review of the current state of film cooling has been provided by Bogard and Thole [4], and a review of the current state of shaped cooling holes in particular was provided by Bunker [5] as a few very broad examples.

Contributed by the International Gas Turbine Institute (IGTI) of ASME for publication in the JOURNAL OF TURBOMACHINERY. Manuscript received January 22, 2017; final manuscript received February 14, 2017; published online April 19, 2017. Editor: Kenneth Hall.

However, among the studies available on film cooling, few investigate the effects of the inlet incidence angle on airfoil film cooling, especially on a stagnation line row of holes. Most commonly, the effect has been studied in leading edge models. An early study by Cruse et al. [6] used a model leading edge with three rows of coolant holes with one row along the stagnation line and one row on either side of the stagnation line row. They observed significant decreases in $\bar{\eta}$ values when the stagnation line was moved above the center row of holes forcing coolant from the center row to move away from the “suction” side. However, when the stagnation line was moved to the bottom of the center row of holes, there was no noticeable increase in $\bar{\eta}$ values despite the increased coolant flow toward the “suction” side. Another leading edge model study done by Wagner et al. [7] used a leading edge model with two rows of holes which were placed at $\pm 3.3d$ from the stagnation line, including a configuration using shaped holes. They found that the adiabatic effectiveness downstream of both rows of holes increased when the approach angle was changed by 5 deg resulting in 1d movement of the stagnation line. Consequently, this study showed the sensitivity to stagnation line position even when the stagnation line did not directly impact the coolant holes.

Additional experiments have investigated the effects of incidence angle on η over varying incidence angles of airfoil models. For example, Ahn et al. [8,9] performed pressure-sensitive paint (PSP) experiments on a simplified three-row cylindrical hole blade model in a rotating rig by varying the rotational speed (no equivalent incidence angles were provided). Since the cooled blade installed in their rotating rig was an extrusion of a two-dimensional airfoil profile, the stagnation line was not properly positioned along parts of the center row of holes. However, Ahn et al. [8,9] found a pronounced increase in the effectiveness on the center row of holes, especially when the stagnation line aligned with the hole. Most recently, Zhang and Yuan [10] studied the combined effects of compound angle shaped holes and varying incidence angle on the showerhead and pressure-side effectiveness of a GE-E3 guide vane at -10 deg, 0 deg, and +10 deg incidence angles with PSP. Zhang found that the peak effectiveness increases with positive incidence angle and also found that the peak effectiveness moved downstream with positive incidence. Zhang also found that the effect of incidence angle is most pronounced at the showerhead region, and although Zhang reported that the pressure distribution downstream of the showerhead region was nearly unchanged, no pressure distributions were provided in the paper. For this study, the suction side of the model was not visible.

It is also worth noting that there is some literature available which presented computationally simulated results of this effect as well. Benabed et al. [11] performed a numerical simulation of a turbine blade with two rows of holes straddling the stagnation line. They observed significant variations in adiabatic effectiveness while incidence angle was varied over a range of ± 10 deg. As a result of the coolant changing sides of the model, a significant enhancement of η is present, at the expense of decreased performance on the other side. For positive incidence angles, the suction side performs quite well. Area-averaged film-cooling effectiveness over the whole blade was the greatest for the most positive (+10 deg) incidence angle shift, which occurred for all blowing ratios.

Matched Biot number testing has recently become a useful analysis method to study airfoil components. Originally developed by Albert et al. [12], it has slowly been expanded upon in studies by Nathan et al. [13], Dees et al. [14], and Dyson et al. [15]. Matched Biot number enables testing of the overall effectiveness, which is the normalized temperature of the operating component, defined as

$$\phi \equiv \frac{T_{\infty} - T_w}{T_{\infty} - T_{c,\text{internal}}} \quad (2)$$

where $T_{c,\text{internal}}$ is the internal temperature of the coolant delivered to the airfoil, and T_w is the temperature at the external surface of the airfoil.

The concept behind overall effectiveness measurements lies in a 3D analysis detailed by Nathan et al. [13]. By considering the steady heat diffusion equation, it can be shown that in order to be able measure ϕ it is critical to match the model Biot number, Bi , the adiabatic effectiveness, η , the warming factor, χ , and the ratio of external and internal heat transfer coefficients, h_f/h_i . Here, Bi is defined as

$$\text{Bi} = \frac{h_f t}{k} \quad (3)$$

and includes the film cooled external heat transfer coefficient, h_f , a reference part thickness, t , and the thermal conductivity, k , of the solid part. If testing a model with a different physical scale of the test component, matching the Bi then requires the selection of a material with an appropriate thermal conductivity, as h_f is determined by the fluid hydrodynamics and t is determined by the factor that the model is scaled by. The warming factor χ accounts for the difference in temperature between the coolant at the base of the model $T_{c,i}$ and the hole exit $T_{c,\text{exit}}$

$$\chi \equiv \frac{T_{\infty} - T_{c,\text{exit}}}{T_{\infty} - T_{c,i}} \quad (4)$$

Matching all of these parameters results in a model which is thermally scaled to the actual engine component, and constructing such a model results in the capability to measure ϕ using a laboratory model that is applicable to actual engine conditions.

There are a number of papers which have investigated adiabatic and overall effectiveness in particular for the showerhead region. Considering research in which the showerhead was studied with no changes in incidence angle, Nathan et al. [13] investigated a five-hole showerhead region in addition to two gill rows and found increasing overall and adiabatic effectiveness levels for the range of momentum flux ratios tested. Dyson et al. [15] studied a complete airfoil which included a showerhead region and also found consistent increases in the overall effectiveness over the range of momentum flux ratios. A companion paper from this study [16] investigates the adiabatic and overall effectiveness in detail for this model over varying blowing ratios and finds the same result for the showerhead region. However, Albert et al. [12] varied incidence angles over a leading edge with forward-diffused shaped holes by ± 3 deg and found little variation in the overall effectiveness even with dramatic changes in adiabatic effectiveness, since change in stagnation line location caused significant effects on the coolant from the stagnation row of holes.

The primary research goals for this study were to investigate the effects of varying incidence angle on the adiabatic and overall effectiveness of a fully cooled model with shaped holes. First, adiabatic effectiveness measurements were made across 150 hole diameters on the fully cooled model in order to investigate the effects of incidence angle on near-stagnation and far downstream regions on the airfoil model. The effects of the stagnation line and incidence angle were then investigated in further detail for only the showerhead region, since the effects were most pronounced at that location. The results serve as a useful reference for understanding the relative cooling effects for showerheads employing impingement geometries, as well as for understanding the effects of utilizing conical holes in the stagnation region of the airfoil.

Experimental Setup

Experimental Facility. All experiments took place in a closed-loop wind tunnel containing a three-airfoil, two-passage linear cascade test section, which can be seen in Fig. 1. The wind tunnel test section measured 1.27 m wide by 0.55 m tall. The center airfoil could be replaced by one of several airfoil models utilized for the project depending on what test was being performed, whereas the outer two airfoils were not instrumented and only matched the

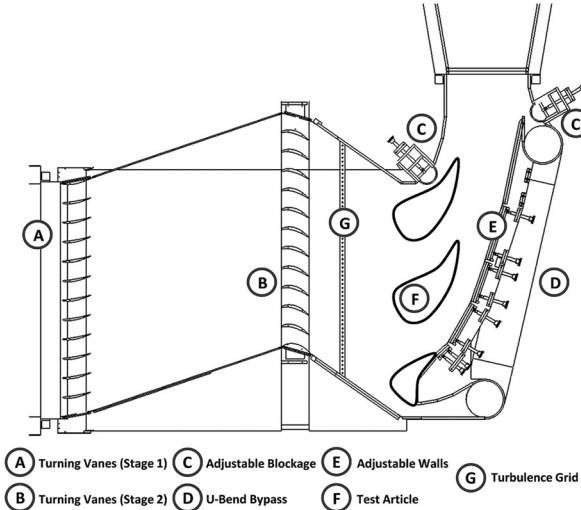


Fig. 1 Schematic of turbine airfoil cascade facility with upstream turning vanes to control approach flow angle: A—turning vanes (stage 1), B—turning vanes (stage 2), C—adjustable blockage, D—U-bend bypass, E—adjustable walls, F—test article, and G—turbulence grid

external surface of the center airfoil. Adjustable walls and bypass flow ducts provided flow control in order to allow positioning the stagnation lines on each airfoil model and setting the pressure distribution on the test airfoil model.

For all tests, the mainstream velocity was set to $U_{\infty,\text{inlet}} = 5.5$ m/s. This yields an inlet Reynolds number of $\text{Re} = 120,000$, where Re is defined with respect to the mainstream velocity and the airfoil model axial chord length as follows:

$$\text{Re} \equiv \frac{U_{\infty,\text{inlet}} C_{\text{ax}}}{v_{\infty}} \quad (5)$$

The wind tunnel was recently upgraded with two sets of upstream turning vane cascade receptacles in which different pairs of turning vane cascades could be installed. The installed turning vane cascade pair redirected the flow into the test section. This flow redirection enabled testing at discrete nonzero inlet incidence angles. Rods downstream of the second turning vane cascade generated mainstream turbulence which decayed to $Tu = 5\%$ at the leading edge of the airfoil model, with an integral length scale of $\Lambda = 6\%$ of the axial chord length. These values were measured upstream with a hot-wire anemometer after it was verified experimentally that the downstream prediction of the turbulence level could be made using a modified version of the Roach correlation [17] (of which the formulation of the correlation is available in Ref. [18]).

For the current study, two pairs (a total of four) of turning vane cascades were used to generate two inlet incidence angles corresponding to 0 deg and -9 deg relative to the design engine incidence angle. These two inlet incidence angles were measured with particle image velocimetry (PIV). First, measurements were made with a particular pair of turning vane cascades installed in the wind tunnel. The PIV laser sheet was aimed in the side of the wind tunnel in order to collect PIV flowfield measurements at the radial mid-span of the wind tunnel far away from the walls. Measurements were made over an area equivalent to about $1/4$ the distance between the turning vanes and the instrumented airfoil. The flowfield measurements were used to calculate incidence angle to about ± 0.2 deg. The turbulence grid was installed, and PIV measurements were then taken downstream of the turbulence rods over 30 rod diameters in order to verify the final inlet incidence angle, since the turbulence rods deflected the turning vane cascade outlet angle slightly. The process was repeated for the additional pair of turning vane cascades as

well as the additional turbulence grid. The inlet incidence angle values reported are those entering the test section downstream of the turbulence rods and they were measured to be nominally -30.1 deg and -21.1 deg, corresponding to the previously stated 0 deg and -9 deg relative to the design engine incidence angle.

The effects of incidence angle were investigated for the adiabatic effectiveness of the model at these two discrete incidence angles. For each incidence angle, five momentum flux ratios were tested. The adiabatic effectiveness of the five momentum flux ratios were compared for the two incidence angles in order to better understand the effects of incidence angle on the adiabatic effectiveness for this airfoil. The adiabatic effectiveness levels in the showerhead region were investigated further by moving the stagnation line across the conical row of holes at the $i = -9$ deg condition at two intermediate momentum flux ratio conditions. Finally, the effects of the incidence angle on the overall effectiveness of the model were tested at one of the momentum flux ratio cases.

Adiabatic effectiveness results are presented using the averaged hole exit temperature of all of the holes in order to provide a continuous effectiveness plot for the fully cooled laterally averaged effectiveness data, which would otherwise be discontinuous if individual hole temperatures were utilized for different holes. Since three feeds were used to provide coolant to the models, the averaged inlet temperature was used as the reference temperature. Finally, laterally averaged effectiveness levels were averaged across the whole viewing area. Since the pitch of the holes changes with respect to the position on the airfoil model, the laterally averaged effectiveness levels therefore are not averaged over an integer number of pitches.

Test Models. For this study, three instrumented airfoils were used. The three airfoil models all had identical external surface curvature and had an axial chord length of $C_{\text{ax}} = 0.355$ m. The two film-cooling models contained the same external and internal geometries. The first model contained 34 pressure taps and was created solely in order to measure the surface pressure distribution. The second and third models were scaled-up midspan extrusions of a film-cooled turbine component and contained internal channels and film cooling holes representative of those used in a film-cooled airfoil component. The second was made of a low-conductivity material for use in adiabatic effectiveness measurements, and the third was manufactured out of a higher conductivity material selected to match Bi to engine conditions.

In order to set the pressure distribution (C_p) and stagnation lines, the first model was inserted into the wind tunnel. This model contained 22 static pressure taps at midspan, 6 at 40% span, and 6 at 60% span. A CFD simulation was performed in order to generate a prediction of the C_p and stagnation line position for an infinite cascade with the tested inlet incidence angle. (For reference, the CFD prediction was modeled in ANSYS FLUENT 15.0, followed standard freestream and near-wall mesh resolution practices and utilized inlet and outlet pressure boundary conditions. The prediction was 2D, used Reynolds-averaged Navier-Stokes equations, and utilized the $k\omega$ -SST turbulence model.) The walls, bypass flow rates, and blockages of the test section were then adjusted until the experiment matched the predictions to within uncertainty. The definition of C_p used for the study was as follows:

$$C_p = \frac{P_{\text{static,airfoil}} - P_{\text{total}}}{P_{\text{static,outlet}} - P_{\text{total}}} \quad (6)$$

C_p values were set to within 0.01, which corresponded to variations in velocity around the model of <3% from the predictions, but were typically within 1%. Stagnation lines were set to within ± 1.5 mm, corresponding to $\pm 0.3 s/D$. A plot of the leading-edge pressure distribution can be seen in Fig. 2. Figure 2 also contains the CFD prediction as discussed previously. For the two incidence angles tested, local velocities vary by less than 7% across the airfoil except in the near-showerhead region. Therefore, although the

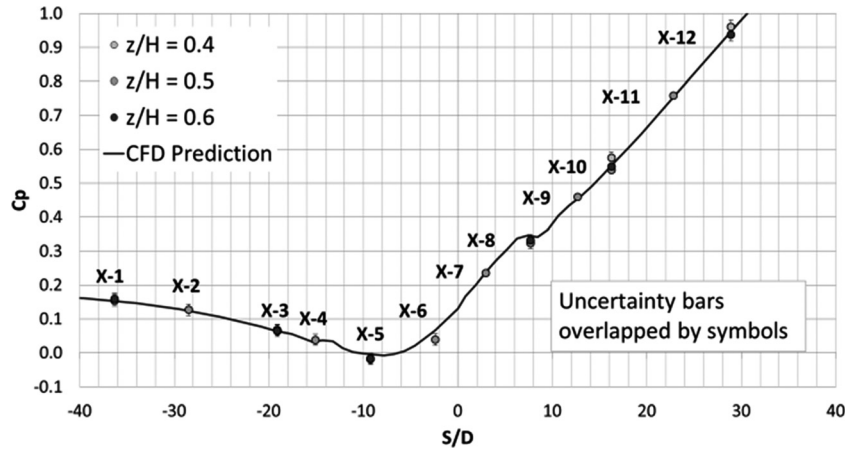


Fig. 2 C_p predictions and measurements in the leading edge region of the airfoil model

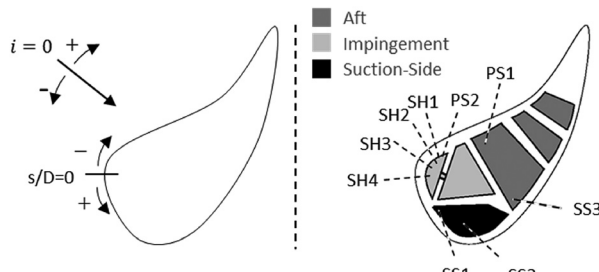


Fig. 3 (Left) airfoil coordinate system. (Right) locations of film cooling holes and internal passages.

change in inlet incidence angle is quite large, and the C_p values were set for each incidence angle, the overall pressure distribution does not vary significantly downstream of the showerhead region.

In order to perform the film cooling experiments, two-film cooled models were utilized. The first model was manufactured from a low conductivity polyurethane foam with $k \sim 0.044 \text{ W/m K}$, which provided a reasonable approximation of an adiabatic surface to use for adiabatic effectiveness measurements. The second model was made out of DuPont™ Corian® ($k \sim 1 \text{ W/m K}$), which was used for the overall effectiveness experiments. Using Eq. (3), it was determined that using Corian provided a Biot number very close to engine conditions. This was verified through CFD as well as earlier experimental work as shown in Chavez et al. [19]. Therefore, Corian was used to manufacture the conducting film-cooled model. The ratio of heat transfer coefficients was matched by manufacturing the foam and Corian models with features identical to the actual engine component. The front internal passage contained an impingement cooling configuration, the suction-side passageway a smooth internal passage, and the aft passage was a three-pass serpentine channel. The front and back passages both contain rib turbulators as used commonly in real turbine components.

A visual representation of the airfoil model can be seen in Fig. 3. A summary of the film-cooling geometry can be seen in Table 1. The four showerhead rows are conical holes, while the other four holes are all standard laidback fan-shaped holes. An average hole diameter (4.9 mm) is used in order to provide contour plots of the data and to examine the effectiveness downstream of the holes.

Coolant Loop. Coolant was supplied to the three internal passages at the base of the airfoil model by a secondary coolant flow loop. This secondary loop was driven by a 7.5 hp blower. Air was drawn from the secondary flow loop by the blower and flowed into

Table 1 Film cooling hole designations

Hole	Type	s/D	d (mm)
PS1	Fan	-46.3	5.4
PS2		-23.8	5.0
SH1	Conical	-16.8	5.0
SH2		-11.7	5.0
SH3		-5.4	5.0
SH4		1.0	4.6
SS1	Fan	14.7	4.7
SS2		35.4	4.7
SS3		59.0	4.6

the coolant heat exchanger, where it was mixed with liquid nitrogen. The cold mixture then was split into the three passages for each main passage within the airfoil. These three passages contained long sections of straight pipe which each contained an orifice flow meter and were each regulated by a valve further downstream. The flow then passed up into an inlet channel whose three passages converted the internal shape from the circular piping to the individual shapes of each internal airfoil channel. Further downstream of the shape transitions, a constant cross section inlet channel of $z/H = 1$ ensured the flow was fully developed as it entered the airfoil model. Note that all flow entering the airfoil model exited through the holes. Figure 4 shows a diagram of the coolant loop.

Experimental Methods and Uncertainty. For the low thermal conductivity model, steady state measurements were recorded at

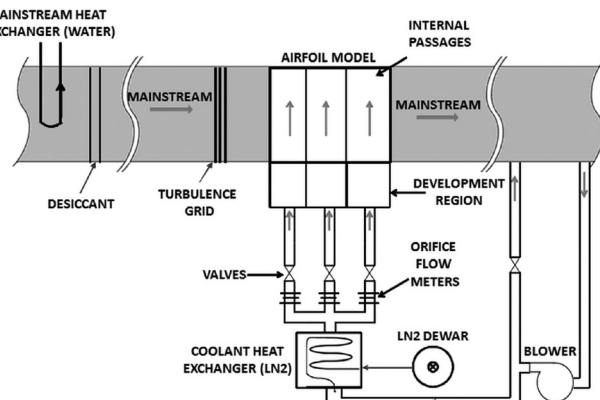


Fig. 4 Schematic of the wind tunnel coolant loop

five flowrate conditions (labeled $I = 0.40$, $I = 1.32$, $I = 2.76$, $I = 4.74$, and $I = 10.38$) and at two incidence angles ($i = 0$ deg and $i = -9$ deg with respect to the nominal operating condition of the airfoil as in Fig. 3). For the matched Biot number model, steady state measurements were recorded at the two incidence angle conditions but only for $I = 4.74$. The follow-up study investigated the effect of the stagnation line on the adiabatic effectiveness at a total of six positions, two of which were the main incidence angles studied, and all of which were made at steady state.

Since the discharge coefficients of each row of holes was measured previously, they could be used in conjunction with the channel mass flow rates and pressure distribution measurements to calculate the momentum flux ratios through each row of holes for each condition tested. The momentum flux ratio is defined as

$$I = \frac{\rho_c U_c^2}{\rho_\infty U_{\infty, \text{local}}^2} \quad (7)$$

where the approach velocity ($U_{\infty, \text{inlet}} = 5.5$ m/s) was used in place of $U_{\infty, \text{local}}$ to determine the momentum flux ratios for the four conical showerhead rows and the pressure-side gill row. Table 2 summarizes the tested conditions.

At the nominal operating incidence angle, the internal pressures at the base of the airfoil model were measured for each condition. The pressures at the inlet of the airfoil model were held constant while changing incidence angles. However, since the external velocities and hole discharge coefficients did not vary significantly between the two incidence angle conditions, the mass flow rates for each condition are also identical. This means that the momentum flux ratios do change slightly for the suction-side and pressure-side holes since the greatest difference in local velocity occur there. The difference in momentum flux ratios for the five pressure- and suction-side rows for the two incidence angles are shown in Table 3.

Although the change in inlet incidence angle changes the stagnation line position to discrete values, a more thorough investigation of the effects of the stagnation line was made at conditions $I = 2.76$ and $I = 4.74$. This was achieved by moving the two blockages in opposite directions by a discrete amount. This has the

intended effect of changing the total flowrate through each blockage passage, therefore affecting the stagnation lines of all three models. During the change, showerhead momentum flux ratios, wind tunnel velocity, and coolant conditions were all held constant. The investigation was performed since there was an obvious sensitivity to the adiabatic effectiveness in the showerhead region while the initial tests were performed.

Surface temperature data were collected simultaneously with five FLIR IR thermographic cameras positioned at various locations around the airfoil as shown in Fig. 5. Cameras viewed the airfoil through NaCl or ZnSe windows to allow for transmission of the temperature data through the otherwise acrylic test section. Collecting the data with five cameras allowed for a continuous view of a significant portion of the airfoil model ($-80 < s/D < 80$ and $z/H = \pm 0.15$) for the full coverage tests. One camera was used to collect the showerhead data when experiments investigated the showerhead region in detail. Both models were coated with matte black paint to ensure a uniform surface emissivity and then fiducial markings were added with a silver paint pen in 6.3-mm increments immediately outside of the where the final data were collected. Utilizing a silver pen ensured that the fiducial marks were visible, as their starkly different emissivities produce false temperature data and are therefore easily visible in the IR images.

IR calibrations were performed for each camera utilizing surface thermocouples affixed to thick copper coupons and thereafter to various locations over or near film cooling holes on the adiabatic effectiveness model. The copper coupons were painted with the same matte black paint used to coat the models. In order to complete the calibration, coolant was run through the foam model, cooling down the copper coupons. IR images and thermocouple temperature data were captured for all IR cameras and thermocouples over a wide range of temperatures. The resulting data were used to generate calibration curves for each camera which varied spatially with s/D location. The calibrations were applied to all IR surface temperature data for any future adiabatic or overall effectiveness experiments.

In order to present data as continuous z/H and s/D plots, data were combined with a data processing algorithm. For each experiment, pinhole camera models were generated utilizing the locations of the fiducial marks in each image for each camera. The fiducial marks were used in conjunction with their true 3D

Table 2 Tested momentum flux ratios for $i=0$ deg

Hole	Condition (average momentum flux ratio)				
	$I = 0.40$	$I = 1.32$	$I = 2.76$	$I = 4.74$	$I = 10.38$
PS1	0.60	1.88	3.85	6.52	13.85
PS2	0.25	0.99	2.35	4.58	11.28
SH1	0.28	1.16	2.67	4.81	10.69
SH2	0.11	0.55	1.65	3.6	8.81
SH3	0.63	2.29	3.93	5.16	9.88
SH4	0.25	1.00	2.44	4.73	10.82
SS1	0.13	0.78	1.92	3.07	7.10
SS2	0.78	1.35	2.15	3.58	6.67
SS3	0.59	1.87	3.88	6.63	14.36

Table 3 Tested momentum flux ratios for $i=-9$ deg for the downstream holes

Hole	Condition (average momentum flux ratio)				
	$I = 0.40$	$I = 1.32$	$I = 2.76$	$I = 4.74$	$I = 10.38$
PS1	0.49	1.52	3.12	5.28	11.22
SS1	0.14	0.86	2.13	3.41	7.88
SS2	0.70	1.22	1.94	3.24	6.04
SS3	0.51	1.62	3.35	5.72	12.39

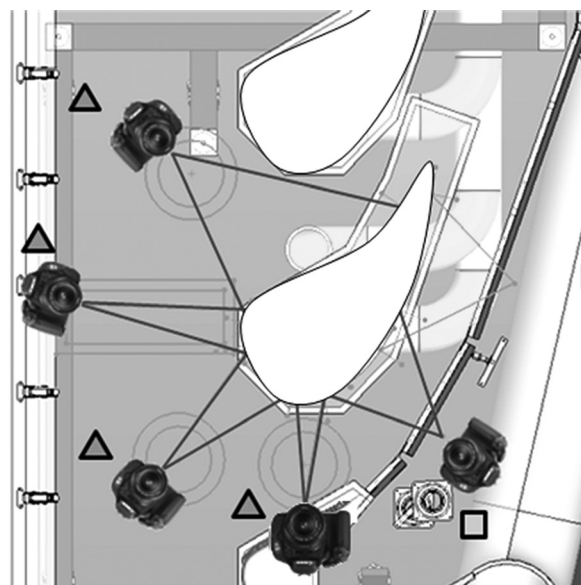


Fig. 5 Camera locations, with triangles indicating cameras on top of the tunnel, and squares indicating cameras beside the tunnel

coordinates in order to generate the camera model. The model was thereafter used to generate a transformation from pixel location to 3D location. A correlation between 3D location to s/D and z/H then flattened out the images. Very thin strips (~ 5 to 10 mm) were interpolated across in overlap regions in order to create continuous contour plots. In all cases, calibrated temperature differences in the overlap regions were within the uncertainty of the calibrations.

Pressures and temperatures were also measured during each test. The adiabatic model contained three gas thermocouples at the root of the airfoil, 15 surface thermocouples at various locations within the model, three pressure taps at the root of the airfoil, and five internal midspan pressure taps. Separate experiments were run to verify that $T_{c,\text{exit}}$ was within 0.5 K of those measured at the root of the airfoil, since gas thermocouples actually located at the hole exits were not permanently mounted into the airfoil. All of these measurements were also made for the overall effectiveness model. In addition, eight internal gas thermocouples were used to measure internal coolant temperatures which allowed determination of χ in each channel.

The mainstream temperature T_∞ was measured by three gas thermocouples located across the test section inlet width. The maximum difference between the three thermocouples was within ± 0.25 K for all tests. The coolant temperature was taken as the average of all three coolant channels, although there was a difference in channel temperatures by as much as 3 K during the tests. For both models, the mainstream temperature was set to $T_\infty = 305$ K, and the coolant temperature to $T_c = 248$ K resulting in a density ratio of $DR_{\text{Avg}} = 1.23 \pm 0.01$ for all tests, where density ratio is defined as

$$DR = \frac{\rho_c}{\rho_\infty} \quad (8)$$

In order to maintain these low coolant temperatures, desiccant was installed upstream of the settling chamber, taking the relative humidity down to manageable levels. Typically, this was anywhere from 1–5% depending on external conditions. It is also worth noting that although this density ratio is low versus engine

conditions, there is evidence to suggest a scalability with momentum flux ratio to engine conditions (such as Sinha et al. [20] and Ethridge et al. [21] for example).

For each momentum flux ratio, three to four rounds of images were taken after reaching steady state, resulting in a total of 15–20 images collected for each momentum flux ratio. Instrument data (pressures, temperatures, flow rates, etc.) was also collected during each image capture. This resulted in 15–20 sets of instrument data for each momentum flux ratio. The images and data were all averaged together in order to create a single input of channel temperatures and flow rates for each momentum flux ratio condition. The scatter within the images as well as the instrument data was under 1% of each reading. These data were used as inputs for the software processing algorithm.

In addition to the previously mentioned calibrations, an additional experiment was completed in order to correct the adiabatic model for conduction errors present since the material is not truly adiabatic. This was achieved by measuring surface temperatures for each camera and for each momentum flux ratio after taping off two to three holes at midspan for each row of holes. Since the coolant passing behind the blocked coolant holes cools down the internal and external surface of the vane, surface temperatures lower than the mainstream temperature are recorded and used for input in to Eq. (1). In this case however, the measurable nonzero η actually represents conduction error present for the partially blocked area. This nonzero η measurement is called the no-film adiabatic effectiveness levels (η_0), and η_0 was combined with the original η data sets to correct the initially measured values based on the following equation:

$$\eta = \frac{\eta_{\text{measured}} - \eta_0}{1 - \eta_0} \quad (9)$$

where η_{measured} is the initially directly measured η with conduction errors present, and η_0 is the no-film adiabatic effectiveness measured in the correction experiment, the derivation of which is presented in Ethridge et al. [21]. The magnitude of the correction had an effect of reducing the adiabatic effectiveness plots from as little as 0.02 to as much as 0.13, but was on average 0.07. Oftentimes,

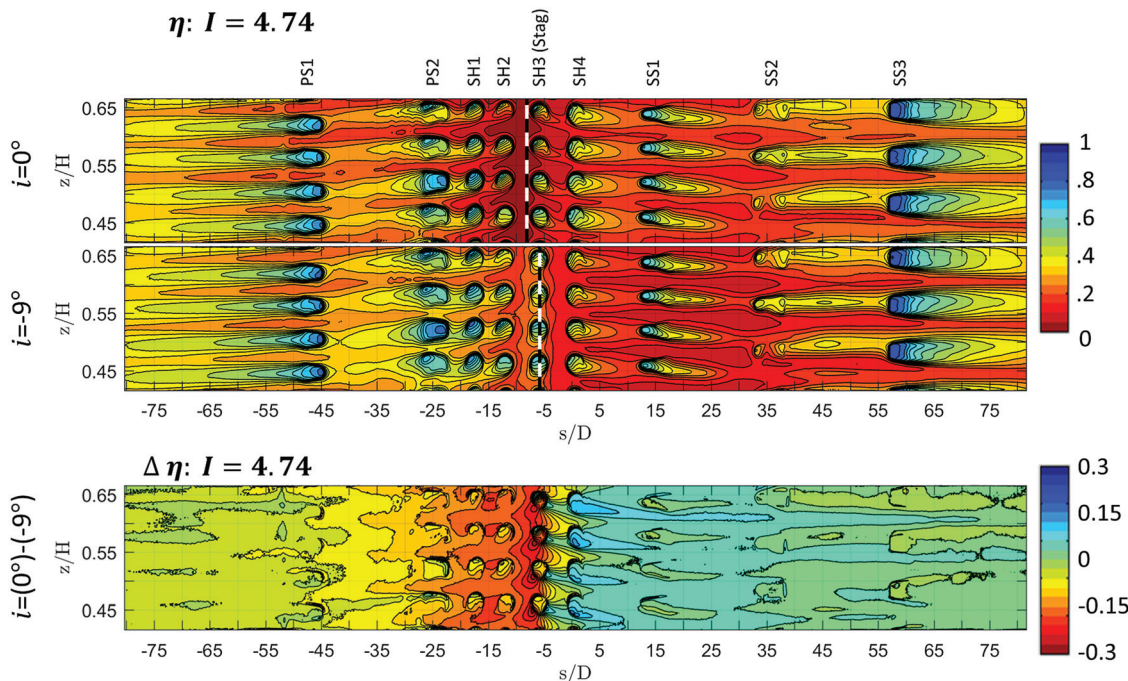


Fig. 6 (Top) adiabatic effectiveness measurements of the airfoil, $i = 0$ deg, $I = 4.74$ with the stagnation line shown. (Middle) adiabatic effectiveness measurements of the airfoil, $i = -9$ deg, $I = 4.74$ with the stagnation line shown. (Bottom) difference in adiabatic effectiveness at the two different incidence angles for $I = 4.74$.

this correction is not applied to the showerhead region, since the conduction is highly 3D near densely packed hole rows. In this case, the correction is still able to remove the 1D component, resulting in more appropriate levels of the reported η .

Precision uncertainty in the overall and adiabatic effectiveness measurements were evaluated through an analysis of the test-to-test repeatability of the measurements after resetting wall position and pressure distribution and reinstalling turning vanes. Precision uncertainty for both η and ϕ were calculated to be $\delta\phi = \delta\eta = \pm 0.02$. The precision uncertainty in the conduction correction was estimated at $\delta\eta_0 < \pm 0.02$, propagating through to a $\delta\eta < \pm 0.005$. Bias uncertainty for DR and I were estimated through sequential perturbation of the elemental uncertainties. For the average density ratio, uncertainty was estimated to be $\delta DR_{Avg} = \pm 0.01$, which included the thermocouple calibration uncertainty and uncertainty in the averaging process for the multiple channel coolant temperatures and mainstream thermocouples. However, bias uncertainty in density ratio for each passage was negligible after calibrating all thermocouples in a high accuracy glycol bath prior to installation. Bias uncertainty in I was estimated at $\delta I < 7\%$ for the lowest momentum flux ratio condition for holes with the worst uncertainty and $\delta I < 5\%$ for all momentum flux ratio conditions thereafter for all holes based off uncertainties in the mainstream velocity reading, the orifice plate and cooling hole discharge coefficients, and measured model hole diameters.

Results and Discussion

Full Coverage Measurements. An overview of the effects of incidence angle with varying momentum flux ratio is presented in Figs. 6 and 7. Figure 6 shows the distributions of adiabatic effectiveness with incidence angles of $i = 0$ deg and -9 deg with coolant jets operated at an average momentum flux ratio of $I_{avg} = 4.7$. Also shown in Fig. 6 is the difference in η values for the two incidence angle cases. The largest difference is clearly in the showerhead and persists strongest up through the gill row of holes on the pressure side of the airfoil. The effect is diminished to $\Delta\eta = 0.05$ halfway between the gill-row and the last pressure side (PS) row for the highest three momentum flux ratio cases.

Finally, Fig. 6 shows the locations of the stagnation lines for each incident angle case. For $i = 0$ deg the stagnation line was located at $s/D = -8$, at the edge of the SH3 holes; while for $i = -9$ deg the stagnation line was located at $s/D = -6$, which was close to the center of the SH3 holes. Interestingly, for a short region on the suction side, the near-stagnation region effectiveness is actually higher than the $i = 0$ deg case even though all of the coolant proceeds to the suction side. This has been seen in some leading edge studies and is presumably due to the inability for the stagnation row to penetrate deeply into the mainstream when the stagnation line is either very near or directly over the holes. As a result, the fluid is redirected back on to the leading

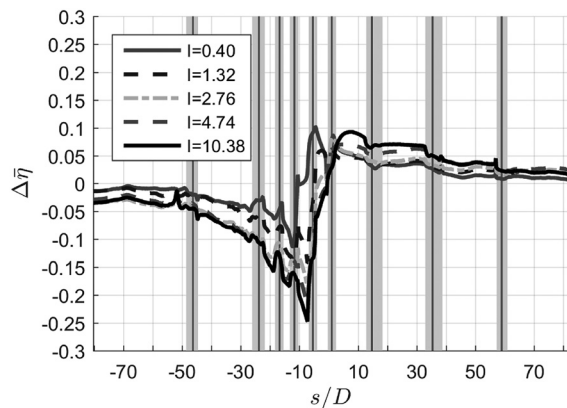


Fig. 7 $\Delta\bar{\eta}$ versus s/D for all momentum flux ratios

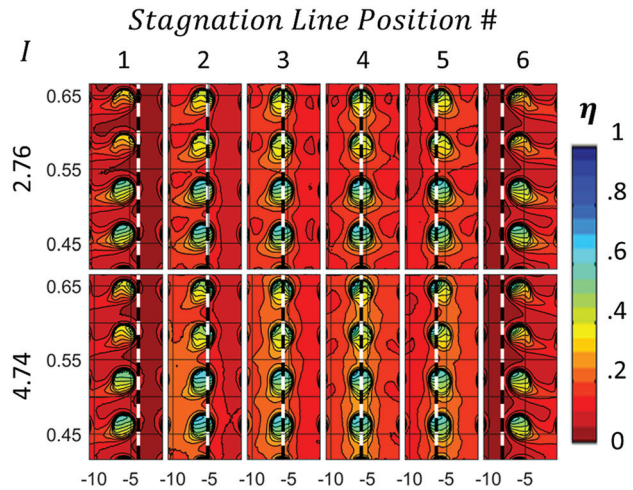


Fig. 8 η for multiple stagnation line positions, showing the effects of stagnation line on conical holes

edge and enhances the adiabatic effectiveness in the near-hole region. Also, the turbulent mixing which is generated due to this interaction transforms the distinct jets into a somewhat uniform blanketing layer, as evidenced by the difference in the effectiveness levels on pressure side. The strength of the enhancement, especially in the showerhead region, prompted the investigations of the effects of the stagnation line on η in the showerhead region.

Figure 7 shows these results in terms of the difference in laterally averaged adiabatic effectiveness, $\Delta\bar{\eta}$. From Fig. 7, it is clear that the difference in incidence angle changes the adiabatic effectiveness predominantly in the showerhead region. Adiabatic effectiveness is enhanced most for row SH3 (located at $s/D = -6$) for the incidence $i = -9$ deg case. The magnitude of the difference in adiabatic effectiveness on the pressure side changes from $\Delta\eta = -0.25$ at $s/D = -6$, to $\Delta\eta = -0.03$ at $s/D = -80$, and changes from $\Delta\eta = +0.1$ at $s/D = 8$, to $\Delta\eta = +0.02$ at $s/D = 80$ on the suction side for the highest momentum flux ratio case. Figure 7 also reveals that there is a total decrease in the adiabatic effectiveness over the 160 hole diameters viewed in the experiments, as the net decrease in adiabatic effectiveness in the showerhead region does not overcome the increase seen downstream on the suction side.

The results from the full-coverage tests imply that for modest incidence angle changes, only the effects of the stagnation hole row need to be taken into account. As the difference in incidence angles increase beyond those studied here, it would become more important to examine the influence due to the changes in the pressure distribution and discharge coefficients in addition to the stagnation line film row. It is also critical to understand the enhancement in the adiabatic effectiveness at the leading edge due to the incidence angle changes for the particular hole type used at the leading edge.

Table 4 Measured inlet incidence angles (**bold**) and estimated inlet incidence angles (normal font) corresponding to position labels

Position	i (deg)
1	—
2	-10
3	-9
4	-8.4
5	-6.6
6	0

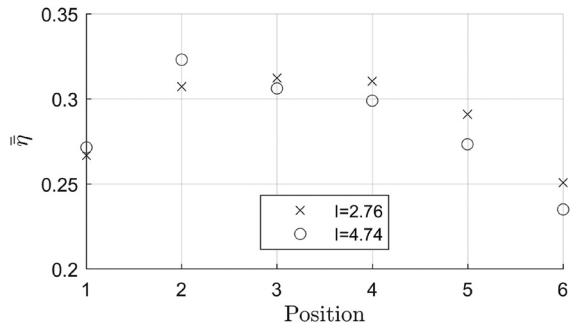


Fig. 9 $\bar{\eta}$ for multiple stagnation line positions, showing the effects of stagnation line on the effectiveness of the showerhead

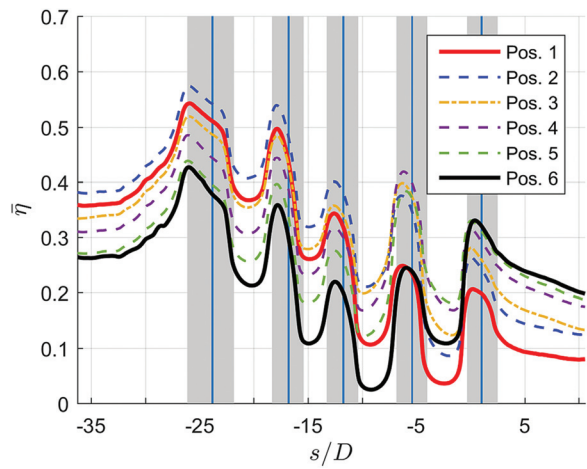


Fig. 10 Laterally averaged adiabatic effectiveness levels for the five stagnation line positions at the average momentum flux ratio condition $I = 4.74$

Effect of Stagnation Line Position. The movement of the stagnation lines is shown in Fig. 8. Furthermore, Table 4 shows the corresponding estimated inlet flow incidence angle tested. For positions other than 3 and 6, which were the incidence angle conditions measured with PIV and stagnation tufts, the inlet incidence angle was estimated by measuring the stagnation line location and

comparing the stagnation line to the CFD generated earlier. Note that position 1 was not measured during the test and so that inlet incidence angle could not be estimated. It is clear that as the stagnation line is passed over the conical holes, there is a significant increase in the near-hole adiabatic effectiveness, especially when the stagnation line is very near the hole. For position 2, $I = 4.74$, the hole jets tend to generate a blanket of coolant immediately downstream of the conical holes. This is a repeatable phenomenon for the conical holes that apparently has a significant effect on the adiabatic effectiveness of the showerhead. It is also clear that the effect occurs for various location beyond the metering hole size but within the footprint of the conical hole shape.

Figure 9 highlights the effect of the stagnation line on the enhancement of $\bar{\eta}$ by taking an average over the whole showerhead region. It can be seen in Fig. 9 that the total average effectiveness, $\bar{\eta}$, is highest for positions 2–4 when the stagnation line is aligned very closely to the hole. It is interesting to note that for position 2, the adiabatic effectiveness for the high momentum flux ratio case is enhanced significantly. Laterally averaged data for the showerhead region is shown in Fig. 10 in order to show the influence of the stagnation line on the laterally averaged effectiveness. The effect is a near step-change on either side of the hole at $s/D \approx -2.5$ and 2.5 . The effect persists far on to the pressure-side showerhead region and beyond the shaped pressure-side gill row, as was seen in the full coverage data. It can be seen that position 2 outperforms all of the other cases in the region near holes PS2, SH1, and SS with a decreased effect beyond $s/D = 0$. However, the effect on the most suction-side part of the showerhead region performs close to that of position 3, which is the $i = 0$ case. Comparing positions 2 and 6 at the left and right bounds of Fig. 10, the effectiveness for position 2 is larger by over $0.1 \bar{\eta}$ on the pressure side, but only lower by about $0.06 \bar{\eta}$ on the suction side.

Overall Effectiveness Measurements. The overall effectiveness distributions for both incident angles at $I_{avg} = 4.74$ are presented in Figs. 11 and 12. It is apparent that there is a change in the overall effectiveness levels for the two incidence angles presented. However, the difference in overall effectiveness on the far pressure side of the showerhead region is only increased by about $\bar{\phi} = 0.05$. The largest effects are seen in the very near-stagnation region, where differences in $\bar{\phi}$ of as much as $\bar{\phi} = 0.1$ are seen at $s/D = -8$. This is coincident with the large enhancement seen in $\bar{\eta}$ for the two incidence angle cases. Therefore, for the case of this particular hole spacing, the adiabatic effectiveness plays a large role in the overall effectiveness at the two incidence angles.

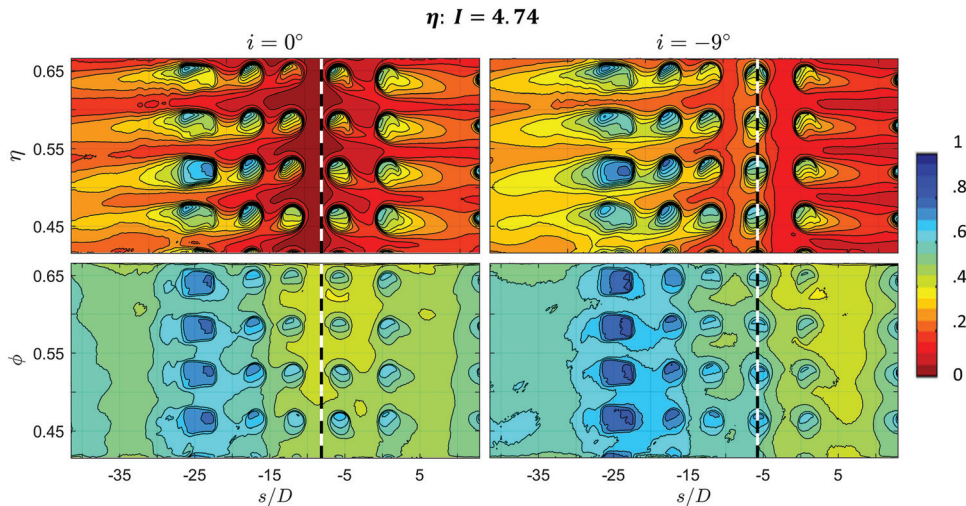


Fig. 11 (Top) Adiabatic effectiveness measurements for the $i = 0$ and $i = -9$ angles at condition $I = 4.74$. (Bottom) Overall effectiveness measurements for the $i = 0$ and $i = -9$ angles at condition $I = 4.74$.

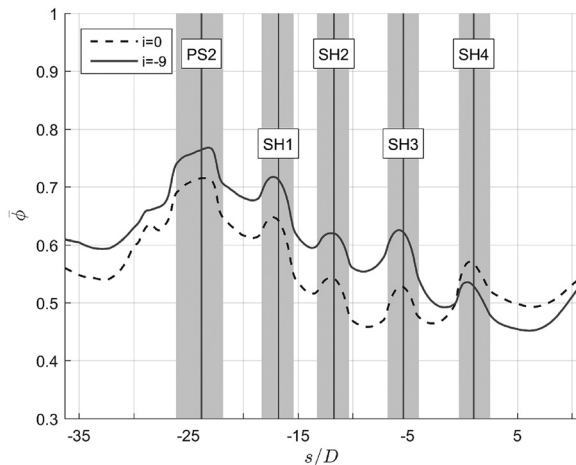


Fig. 12 Laterally averaged ϕ for the two incidence angles studied ($I = 4.74$)

The momentum flux ratios (and hence the internal heat transfer coefficient magnitudes) for the two overall effectiveness data sets are identical, and so the changes in overall effectiveness are due to the adiabatic effectiveness, external heat transfer coefficient, and heat transfer coefficient augmentation levels of the jets. It was shown in a previous study [19] that the no-film heat transfer coefficient is largely unaffected by this magnitude of incidence angle change. Thus, the largest effects are due to the augmentation in heat transfer coefficient as well as the adiabatic effectiveness. Furthermore, the overall effectiveness on the whole is higher for the off-design $i = -9$ deg case due to the enhancement in the showerhead region because the stagnation line was positioned over a row of coolant holes.

Conclusions

The adiabatic effectiveness of a fully cooled turbine airfoil model which contained only shaped holes and with realistic internal heat transfer coefficient augmentors was tested at five momentum flux ratio conditions and two incidence angles 10 deg apart. Film-cooled models were manufactured to test both adiabatic and overall effectiveness. The adiabatic effectiveness airfoil was manufactured out of a low thermal conductivity polyurethane foam, while the overall effectiveness model was made out of DuPont Corian® which allowed for matched Biot number testing. As the momentum flux ratio was increased, the magnitude of the difference between the two incidence angles constantly increased. The effect was most notable in the showerhead region, with differences in the adiabatic effectiveness of $\Delta\eta = 0.3$ visible for the highest momentum flux ratio case. The effect persisted far downstream of the holes to about 45 hole diameters on the pressure side, and about 15 hole diameters on the suction side, although the effect was most magnified on the pressure side, since for the $i = -9$ deg case, the stagnation row of holes had not completely switched to the pressure side.

The adiabatic effectiveness increased by as much as $\bar{\Delta}\eta = 0.17$ when the stagnation line was set immediately near or on top of the breakout of the conical hole shape for the stagnation row of holes and for $I = 4.74$ (as shown in Fig. 10). The effect persisted far downstream beyond the pressure-side gill row, with an enhancement of as much as $\bar{\Delta}\eta = 0.11$. Although this effect has been shown for some cylindrical holes, the effect seems to take place for a larger area around the conical holes due to the increased external footprint.

Finally, ϕ for the $i = 0$ deg case was compared to the $i = -9$ deg case at a moderate momentum flux ratio of $I = 4.74$. Changes in ϕ as large as 0.1 occurred near the stagnation hole row, which was attributed to changes in the η distributions.

Therefore, for the hole spacing presented here, the performance in adiabatic effectiveness played a measurable role in the overall effectiveness compared to the through hole convective cooling and internal impingement cooling.

Acknowledgment

This work was sponsored in part by the Office of Naval Research under Contract No. N00014-09-D-0821/0006.

Nomenclature

Bi	= Biot number
C	= coefficient or chord length
d	= individual hole diameter
D	= average hole diameter
DR	= density ratio
h	= heat transfer coefficient
H	= blade model height
i	= inlet flow angle with respect to nominal
I	= momentum flux ratio
k	= thermal conductivity
P	= pressure
PS	= pressure side
Re	= Reynolds number
s	= curve length coordinate
SH	= showerhead
SS	= suction side
t	= thickness
T	= fluid temperature
Tu	= turbulence intensity
U	= velocity
z	= spanwise coordinate

Greek Symbols

η	= adiabatic effectiveness
Λ	= integral length scale
ϕ	= overall effectiveness
χ	= warming factor

Subscripts, Superscripts, and Accents

avg	= average
aw	= measured at the external adiabatic wall
ax	= airfoil axial distance
c	= coolant
exit	= measured at the hole exit
f	= measured with film cooling
inlet	= measured at the test section inlet
internal	= measured at the airfoil inlet
local	= measured locally
p	= predicted or pressure
static	= static pressure measurement
total	= total pressure measurement
w	= measured at the external wall
0	= measured without film cooling
$\bar{\cdot}$	= laterally averaged
$\bar{\bar{\cdot}}$	= averaged both laterally and streamwise
∞	= mainstream

References

- [1] Goldstein, R. J., 1971, "Film Cooling," *Adv. Heat Transfer*, **7**(1), pp. 321–379.
- [2] Goldstein, R. J., Eckert, E. R. G., and Ramsey, J. W., 1968, "Film Cooling With Injection Through Holes: Adiabatic Wall Temperatures Downstream of a Circular Hole," *ASME J. Eng. Power*, **90**(4), pp. 384–395.
- [3] Hartnett, J. P., Birkebak, R. C., and Eckert, E. R. G., 1961, "Velocity Distributions, Temperature Distributions, Effectiveness and Heat Transfer for Air Injected Through a Tangential Slot Into a Turbulent Boundary Layer," *ASME J. Heat Transfer*, **83**(3), pp. 293–305.
- [4] Bogard, D. G., and Thole, K. A., 2005, "Gas Turbine Film Cooling," *J. Propul. Power*, **21**(6), p. 24.
- [5] Bunker, R. S., 2005, "A Review of Shaped Hole Turbine Film-Cooling Technology," *ASME J. Heat Transfer*, **127**(4), pp. 441–453.

- [6] Cruse, M. W., Yuki, U. M., and Bogard, D. G., 1997, "Investigation of Various Parametric Influences on Leading Edge Film Cooling," *ASME* Paper No. GT-97-296.
- [7] Wagner, G., Ott, P., Vogel, G., and Naik, S., 2007, "Leading Edge Film Cooling and the Influence of Shaped Holes at Design and Off-Design Conditions," *ASME* Paper No. GT2007-27715.
- [8] Ahn, J., Schobeiri, M. T., Han, J. C., and Moon, H.-K., 2007, "Effect of Rotation on Leading Edge Region Film Cooling of a Gas Turbine Blade With Three Rows of Film Cooling Holes," *Int. J. Heat Mass Transfer*, **50**(1–2), pp. 15–25.
- [9] Ahn, J., Schobeiri, M. T., Han, J., and Moon, H., 2004, "Film Cooling Effectiveness on the Leading Edge of a Rotating Turbine Blade," *ASME* Paper No. IMECE2004-59852.
- [10] Zhang, Y., and Yuan, X., 2012, "Effect of Incidence Angle on Gas Turbine First-Stage Nozzle Guide Vane Leading Edge and Gill Region Film Cooling," *ASME* Paper No. GT2012-69298.
- [11] Benabed, M., Azziz, A., and Jubran, B. A., 2010, "Numerical Investigation of the Influence of Incidence Angle on Asymmetrical Turbine Blade Model Showerhead Film Cooling Effectiveness," *Heat Mass Transfer*, **46**(8), pp. 811–819.
- [12] Albert, J. E., Bogard, D. G., and Cunha, F., 2004, "Adiabatic and Overall Effectiveness for a Film Cooled Blade," *ASME* Paper No. GT2004-53998.
- [13] Nathan, M. L., Dyson, T. E., Bogard, D. G., and Bradshaw, S. D., 2014, "Adiabatic and Overall Effectiveness for the Showerhead Film Cooling of a Turbine Vane," *ASME J. Turbomach.*, **136**(3), p. 031005.
- [14] Dees, J. E., Bogard, D. G., Ledezma, G. A., and Laskowski, G. M., 2011, "Overall and Adiabatic Effectiveness Values on a Scaled Up, Simulated Gas Turbine Vane: Part I—Experimental Measurements," *ASME* Paper No. GT2011-46612.
- [15] Dyson, T. E., McClintic, J. W., Bogard, D. G., and Bradshaw, S. D., 2013, "Adiabatic and Overall Effectiveness for a Fully Cooled Turbine Vane," *ASME* Paper No. GT2013-94928.
- [16] Chavez, K., Slavens, T. N., and Bogard, D., 2016, "Effects of Internal and Film Cooling on the Overall Effectiveness of a Fully Cooled Turbine Airfoil With Shaped Holes," *ASME* Paper No. GT2016-57992.
- [17] Roach, P. E., 1987, "The Generation of Nearly Isotropic Turbulence by Means of Grids," *Int. J. Heat Fluid Flow*, **8**(2), pp. 82–92.
- [18] Mosberg, N. A., 2013, "Experimental Investigation of the Performance of a Fully Cooled Gas Turbine Vane With and Without Mainstream Flow and Experimental Analysis Supporting the Redesign of a Wind Tunnel Test Section," *M.S. thesis*, The University of Texas at Austin, Austin, TX, pp. 79–107.
- [19] Chavez, K. F., Packard, G. R., Slavens, T. N., and Bogard, D. G., 2016, "Experimentally Determined External Heat Transfer Coefficient of a New Turbine Airfoil Design at Varying Incidence Angles," International Symposium on Transport Phenomena and Dynamics of Rotating Machinery (*ISROMAC*), Honolulu, HI, Apr. 10–15.
- [20] Sinha, A. K., Bogard, D. G., and Crawford, M. E., 1991, "Film-Cooling Effectiveness Downstream of a Single Row of Holes With Variable Density Ratio," *ASME J. Turbomach.*, **113**(3), pp. 442–449.
- [21] Ethridge, M. I., Cutbirth, J. M., and Bogard, D. G., 2001, "Scaling of Performance for Varying Density Ratio Coolants on an Airfoil With Strong Curvature and Pressure Gradient Effects," *ASME J. Turbomach.*, **123**(2), pp. 231–237.